Proceedings of the 28th IEEE
EMBS Annual International Conference
New York City, USA, Aug 30-Sept 3, 2006

Design and Validation of a Robotic Needle Positioning System for Small Animal Imaging Applications

Adam C. Waspe, *Student Member, IEEE,* H. Jason Cakiroglu,
James C. Lacefield, *Member, IEEE,* and Aaron Fenster, *Member, IEEE*

***Abstract*— A needle-positioning robot has been developed for image-guided interventions in small animals. The device is designed to position a needle with an error ≤ 100 μm. The robot has two rotational axes (pitch and roll) to control needle orientation, and one linear axis to perform needle insertion. The three axes intersect at a single point, creating a remote center of motion. Needle positioning error was quantified at ten target locations for each rotational plane. The measured needle positioning accuracy in free space was 54 ± 12 μm and 91 ± 21 μm for the pitch and roll axes, respectively. The device's accuracy compares favorably with the sizes of typical interventional targets in mouse models.**

***Index Terms*— image-guided intervention, medical robotics, percutaneous needle insertion, three-dimensional imaging, pre-clinical imaging.**

I. Introduction

Biomedical research using preclinical animal models often requires interventions with needles to be performed. This could involve injecting cells [1]–[4], therapeutics [5], or contrast agents [6] to specific organs and vessels within the animal. It could also involve aspiration biopsy of suspicious lesions [1].

For interventions with mice, a reasonable needle positioning accuracy is about $100 - 200$ μm in order to target small tumors [1] and vessels [7]. If targeting is inaccurate, the results can be inconclusive, causing an increase in the number of mice required to perform a study, which increases the time spent and the costs associated with developing treatments.

To improve the accuracy of targeting objects within small animals, some investigators have used high-frequency ultrasound imaging for guiding manual needle insertion procedures [2]–[4], [6]. This method allows the target to be located within the animal and enables visualization of the needle in real time as it is inserted into the tissue.

One problem with image-guided techniques is that there is often an unknown relationship between the coordinate systems of the image and the needle, meaning that it can be difficult to determine the physical location of targets within the animal. Another source of error with this technique is that the needle may not be perfectly in plane with the 2-D image, causing a misinterpretation of the location of the needle tip [8].

To resolve these issues, we have developed a robotic mechanism to perform interventions in small animals. The robotic needle insertion device can be interfaced with a 3-D micro-imaging system, allowing the coordinates of targets found in the image to be registered with the physical coordinate system of the robot. Three-dimensional imaging can be used for target visualization, insertion planning, and validation of the location of the needle placement after insertion [8].

Needle insertion is a constrained procedure involving three decoupled tasks [9]: (1) selection of the needle insertion point, which involves moving the needle tip to the insertion point on the surface of the skin; (2) selection of the needle trajectory or line of insertion, which involves orienting the needle in three dimensions by pivoting at the skin entry point; and (3) insertion of the needle along a linear trajectory until the target is reached. For a robotic device, these tasks can be divided into separate mechanical movements to ensure that the orientation of the needle does not change abruptly during insertion, minimizing damage to the tissue. An innovative design by Taylor *et al.* [10] allows the task of 3-D needle orientation and needle insertion to be mechanically decoupled using a remote center of motion (RCM) approach. With the RCM design, a single point in 3-D space acts as a pivot point for the orientation of the needle. By positioning the needle tip at the RCM, the needle tip can be pivoted at the skin-entry point. Manipulating the location of the RCM moves the location of the skin-entry point.

In this paper, we apply the RCM approach to design a robotic needle placement device for performing needle placement procedures in mice. We describe the design of the system and the implementation of the RCM technique. We explain the calibration techniques used to ensure that an RCM is achieved, and the experimental validation of needle positioning accuracy and precision. We also discuss possible modalities that could be used for image guidance for this system, with emphasis on using 3-D high-frequency ultrasound due to its near-real-time imaging capability.

II. Materials and Methods

A. Robot System Description

Our manipulator robot, as shown in the 3-D computer-aided design (CAD) model in Fig. 1, uses two parallel four-bar linkages arranged in a parallelogram structure to produce a remote center of motion [10]. The two rotational joints of

The authors acknowledge financial support from the Canada Foundation for Innovation, the Ontario Innovation Trust, and the Ontario Research and Development Challenge Fund. A. C. Waspe acknowledges funding from the Natural Sciences and Engineering Research Council of Canada, and the Western Graduate Research Scholarship Program. A. Fenster holds a Tier 1 Canada Research Chair in Biomedical Engineering and acknowledges the support of the Canada Research Chair Program.

The authors are with the Univeristy of Western Ontario, London, ON N6A 5B9, Canada, and Robarts Research Institute, London, ON N6A 5K8, Canada. (email: awaspe@imaging.robarts.ca)

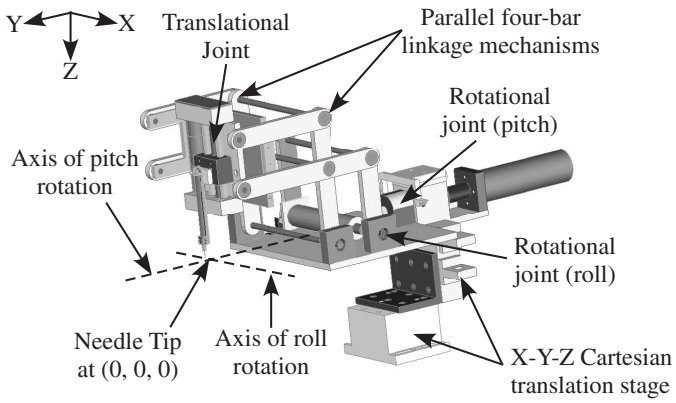

Fig. 1. Three-dimensional CAD model of the needle-positioning robot.

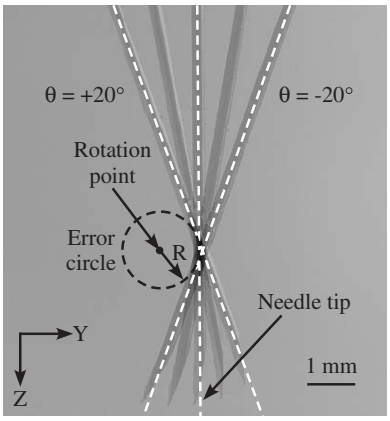

Fig. 2. Composite photograph showing the needle at 5 orientations overlaid on one another. The needle centerlines circumscribe at a distance R from the rotation point. This creates an error circle for the needle axis.

the robot control needle orientation and correspond to pitch and roll angles. The third joint linearly translates the needle to perform the insertion. The four-bar linkage mechanism translates the roll axis of rotation from the actuator to a remote axis that intersects the pitch axis and the linear axis of the needle. The three intersecting axes create an RCM point that acts as a fulcrum for the 3-D orientation of the needle. When the needle tip is placed directly on the surface of the animal, it can pivot about the skin entry point to permit the 3-D orientation of the needle to be manipulated without breaking the skin. The needle tip can reach points that are along a linear trajectory from the RCM.

All joints of the robot are actuated by computer-controlled DC servomotors and are each driven by a linear drive motion controller. These motion controllers are programmed and operated using ASCII commands sent serially from a PC computer via an RS–232 connection. Robot-control software permits needle tip positioning in both Cartesian and spherical coordinates. It includes a graphical user interface and a motion control library that enables the user to input the coordinates of the target and perform system calibration. The forward and inverse kinematic equations of the system are embedded in the software. The software converts coordinates input by the user and performs the necessary kinematic calculations and low-level motor control in order to complete the motion.

B. System Calibration

In order for the system to achieve high positioning accuracy, calibration is necessary to ensure that the three kinematic axes of the robot and the needle tip intersect at a single point. If the needle tip is not placed directly at the RCM point before an intervention begins, the location of the tip will be inconsistent with the kinematics of the robot.

Calibration of the robot was performed using a CCD camera with a high-resolution macro lens. The 3-D position of the RCM was located separately in two orthogonal image planes. The camera was positioned so that the image planes were perpendicular to the rotational axis being calibrated. The RCM was measured with respect to each rotational axis by finding the center of rotation of the centerline of the needle as the needle was positioned at specific angles within the image plane.

The calibration was performed by rotating the needle to specific angles within the image plane. Images of the needle were acquired after each programmed move so that the needle centerline location could be segmented and measured at each angular position.

A set of needle centerlines, located at 0° and $\pm 30^\circ$ for the pitch axis and 0° and $\pm 20^\circ$ for the roll axis, were analyzed to find the center of rotation by treating each centerline as a tangent to an error circle. Fig. 2 shows a set of needle centerlines and the resulting error circle for the roll axis; two additional needles at $\pm 10^\circ$ are shown for display purposes only. The centerlines in Fig. 2 circumscribe a point a distance R from each centerline, indicating that the needle is not calibrated to the RCM in this example. Exterior angle bisectors of the three needle centerlines intersect at the RCM point. The intersection of the two outermost bisecting lines allows for the location of the RCM point with respect to each axis to be calculated.

The horizontal and vertical location of the needle tip was adjusted within the image plane until the radius of the error circle converged to zero. This procedure was performed iteratively for both image planes until the needle tip was located at the RCM point. A more detailed description of this calibration procedure can be found in [11].

C. Validation of Needle Positioning Accuracy

After calibrating the robot, the accuracy of needle tip positioning was quantified to determine if the system met the initial design criteria of being able to reliably position the tip with an error ≤ 100 μm. The error was characterized in free space in order to evaluate the design and calibration of the robot without introducing errors intrinsic to performing an intervention into tissue, such as needle deflection and tissue deformation [12]. The CCD camera was used for determining the positioning error with respect to the pitch and roll axes independently. The needle tip was moved to specific locations relative to the RCM point in the plane of

rotation (which is in plane with the image). Images acquired after each move were used to manually locate the needle tip relative to the RCM point and were compared with the target locations.

Ten target locations were used for each plane of needle positioning. For the pitch axis, the needle tip was placed at $\pm 30\,^{\circ}$, $\pm 15\,^{\circ}$, and $0\,^{\circ}$ at depths of 3 mm and 6 mm below the RCM. For the roll axis, the needle tip was placed at $\pm 20\,^{\circ}$, $\pm 10\,^{\circ}$, and $0\,^{\circ}$ at depths of 3 mm and 6 mm below the RCM. A maximum depth of 6 mm was chosen to maintain the needle tip and edges within the field of view of the camera so that moving the camera during the measurements was avoided.

The local mean and standard deviation (SD) of the error in positioning the needle tip at the corresponding targeted position were estimated for the pitch axis in both the horizontal and vertical image directions (x, z) as:

$$\varepsilon_{xm} = \mu_{xm} \pm \sigma_{xm} = \sum_{i=1}^{N} \frac{x_i}{N} \pm \sqrt{\sum_{i=1}^{N} \frac{\left(x_i - \mu_{xm}\right)^2}{N-1}}, \quad (1)$$

$$\varepsilon_{zm} = \mu_{zm} \pm \sigma_{zm} = \sum_{i=1}^{N} \frac{z_i}{N} \pm \sqrt{\sum_{i=1}^{N} \frac{\left(z_i - \mu_{zm}\right)^2}{N-1}}, \quad (2)$$

where μ_{xm} (μ_{zm}) and σ_{xm} (σ_{zm}) are the mean and SD of the horizontal, x-component (vertical, z-component) error at the m^{th} target location, x_i and z_i are the horizontal and vertical coordinates for the i^{th} measurement at each target point during pitch positioning, respectively, and the number of repeat measurements was $N = 10$. The magnitude distance error and its SD were calculated by adding the x and z component errors in quadrature.

$$\mu_m = \sqrt{\mu_{xm}^2 + \mu_{zm}^2} \quad (3)$$

$$\sigma_m = \sqrt{\sigma_{xm}^2 + \sigma_{zm}^2} \quad (4)$$

This same procedure was performed for the roll axis positioning by replacing x with y.

Once the local accuracy and precision of each target point was quantified individually, the global accuracy, μ_{total}, of the needle positioning system was calculated from the means and standard deviations of the individual local point accuracies using (5). The global SD, σ_{total}, was calculated as the root-mean-square of the individual local point standard deviations using (6).

$$\begin{aligned} \mu_{total} &= \overline{\mu}_m \pm \sigma\left(\mu_m\right) \\ &= \sum_{m=1}^{M} \frac{\mu_m}{M} \pm \sqrt{\sum_{m=1}^{M} \frac{\left(\mu_m - \overline{\mu}_m\right)^2}{M-1}} \quad (5) \\ \sigma_{total} &= \sqrt{\sum_{m=1}^{M} \frac{\sigma_m^2}{M}} \quad (6) \end{aligned}$$

The number of target locations was $M = 10$. Separate global positioning accuracies and precisions were determined for each Cartesian direction and for the magnitude distance error.

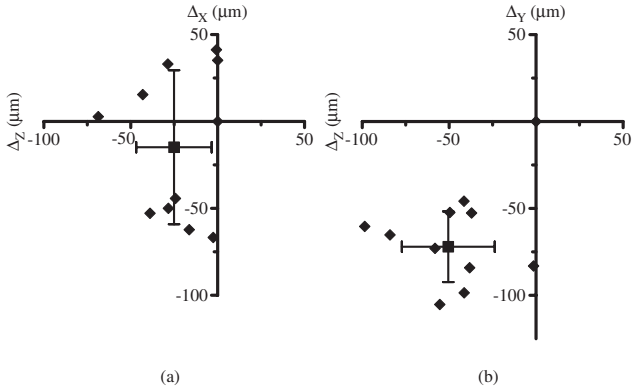

Fig. 3. Needle positioning errors with respect to (a) pitch axis; (b) roll axis. Diamond points represent individual errors and squares represent the mean global error. Error bars represent one standard deviation from the mean global error.

III. Results

Fig. 3(a) shows the error for positioning the needle tip at the individual target points in the pitch (x, z) plane and the global positioning error. The maximum positioning error in the x-direction was -69 ± 8 μm and the maximum error in the z-direction was -67 ± 10 μm. The global error in the (x, z) plane was -25 ± 22 μm in the x-direction and -15 ± 44 μm in the z-direction.

The mean and SD of the magnitude distance error was calculated using (5) and (6), respectively. The global mean accuracy and precision in the pitch axis plane were 54 ± 12 μm and 15 μm, respectively. The maximum magnitude distance error in targeting points in the pitch axis plane was 69 ± 14 μm.

Fig. 3(b) shows the error for positioning the needle tip at individual target points in the roll (y, z) plane and the global positioning error. The maximum positioning error in the y-direction was -98 ± 11 μm and in the z-direction was -105 ± 14 μm. The global error in the (y, z) plane was -51 ± 27 μm in the y-direction and -72 ± 20 μm in the z-direction.

The global mean accuracy and precision in the roll axis plane were 91 ± 21 μm and 17 μm, respectively. The maximum magnitude distance error in targeting points in the roll axis plane was 119 ± 18 μm.

IV. Discussion

A device to deliver therapies and material accurately and reliably to specific locations in small animal research models would be an important tool for pre-clinical laboratory investigations. We have developed a robotic needle placement device, which is designed to be interfaced with a three-dimensional micro-imaging system that is capable of placing a needle tip in free space with a worst case positioning error < 120 μm.

The individual data points in Fig. 3 represent the systematic error of needle tip positioning to a limited number of locations within the workspace of the robot. Systematic errors are associated with the design, manufacturing, and

calibration of the robot. The experimental needle tip positioning results demonstrated that the average overall magnitude distance error in positioning the needle tip was 54 ± 12 μm for the pitch axis plane and 91 ± 21 μm for the roll axis plane.

Random error in measuring the needle tip location is not likely to be a source of error in view of the high precision in needle placement and measurement (15 μm and 17 μm for the pitch and roll axes, respectively). Another source of error could be random error in the calibration measurement.

The high accuracy and precision achieved with this robotic needle positioning device make it an ideal device to interface with a three-dimensional micro-imaging system. High-frequency ultrasound is a good candidate for image guidance of the robot due to its real-time frame rate for 2-D images, high spatial resolution [13], and limited amount of hardware required within the working area of the robot. Three-dimensional images can be constructed by acquiring parallel slices of 2-D images at a predetermined step size in the out-of-plane direction [1], [14]. In our lab, we are able to acquire 3-D images at a rate of 10 slices per second, meaning that a typical 200 slice 3-D image of a mouse liver metastasis can be acquired in 20 s [1]. Combining the needle placement device with the near-real-time 3-D imaging capabilities of high-frequency ultrasound would allow for continual monitoring of tissue deformation and intra-procedural adjustments of the needle trajectory throughout the intervention.

This device could also be interfaced with X-ray micro-computed tomography (micro-CT), since micro-CT also has the high spatial resolution necessary for targeting specific features in small animals [15]. Although the acquisition time of 3-D micro-CT technology is decreasing, the image reconstruction currently cannot be performed rapidly enough to enable visualization of the needle insertion in 3-D throughout a procedure. Another issue with micro-CT is that the robot would have to operate within the confines of a small imaging bore. This constraint would make the mechanical integration between the manipulator robot and the imaging system more difficult. The same problem would be present if magnetic resonance imaging (MRI) were to be used for interventional guidance. Furthermore, the materials used for the construction of the current robot are not compatible for use with MRI.

V. Conclusion

We have demonstrated the design and characterization of a needle placement device that is capable of a positioning accuracy sufficient for performing percutaneous procedures on mice. The mean overall error for positioning the needle tip in free space was 54 ± 12 μm for the pitch axis plane and 91 ± 21 μm for the roll axis plane. This result indicates that the device is suitable for performing needle interventions in small animals.

Acknowledgment

The authors would like to thank C. Blake, G. Mills, J. Montreuil and H. Nikolov for machine shop support, and S. Sherebrin for programming support.

References

[1] K. C. Graham, L. A. Wirtzfeld, L. T. MacKenzie, C. O. Postenka, A. C. Groom, I. C. MacDonald, A. Fenster, J. C. Lacefield, and A. F. Chambers, "Three-dimensional high-frequency ultrasound imaging for longitudinal evaluation of liver metastases in preclinical models", *Cancer Res.*, vol. 65, no. 12, pp. 5231–5237, 2005.

[2] M. L. Springer, R. E. Sievers, M. N. Viswanathan, M. S. Yee, E. Foster, W. Grossman, and Y. Yeghiazarians, "Closed-chest cell injections into mouse myocardium guided by high-resolution echocardiography", *Am. J. Physiol. Heart Circ. Physiol.*, vol. 289, no. 3, pp. H1307–H1314, 2005.

[3] A. Liu, A. L. Joyner, and D. H. Turnbull, "Alteration of limb and brain patterning in early stage mouse embryos by ultrasound-guided injection of Shh-expressing cells", *Mech. Dev.*, vol. 75, no. 1, pp. 107–115, 1998.

[4] J. C. Slevin, L. Byers, M. Gertsenstein, D. Qu, J. Mu, N. Sunn, J. C. P. Kingdom, J. Rossant, S. L. Adamson, "High resolution ultrasound-guided microinjection for interventional studies of early embryonic and placental development in vivo in mice", *BMC Dev. Biol.*, vol. 6, article 10, 2006.

[5] K. Kanoh, T. Shimura, H. Suzuki, K. Nomoto, T. Asao, and H. Kuwano, "Antitumor effect of a splenic injection of 5-fluorouracil on metastatic liver cancer in mice", *J. Pharmacol. Exp. Ther.*, vol. 308, no. 1, pp. 168–174, 2004.

[6] Y. Q. Zhou, L. Davidson, R. M. Henkelman, B. J. Nieman, F. S. Foster, L. X. Yu, and X. J. Chen, "Ultrasound-guided left-ventricular catheterization: A novel method of whole mouse perfusion for microimaging", *Lab. Invest.*, vol. 84, no. 1, pp. 385–389, 2004.

[7] A. A. Pérez-Rivera, G. D. Fink, and J. J. Galligan, "Increased reactivity of murine mesenteric veins to adrenergic agonists: functional evidence supporting increased α_1 – adrenoceptor reserve in veins compared with arteries", *J. Pharmacol. Exp. Ther.*, vol. 308, no. 1, pp. 350–357, 2004.

[8] K. J. M. Surry, W. L. Smith, L. J. Campbell, G. R. Mills, D. B. Downey, and A. Fenster, "The development and evaluation of a three-dimensional ultrasound-guided breast biopsy apparatus", *Med. Image Anal.*, vol. 6, no. 3, pp. 301–312, 2002.

[9] K. Masamune, G. Fichtinger, A. Patriciu, R. C. Susil, R. H. Taylor, L. R. Kavoussi, J. H. Anderson, I. Sakuma, T. Dohi, and D. Stoianovici, "System for robotically assisted percutaneous procedures with computed tomography guidance", *Comp. Aid. Surg.*, vol. 6, no. 6, pp. 370–383, 2001.

[10] R. H. Taylor, J. Funda, B. Eldridge, K. Gruben, D. LaRose, S. Gomory, M. Talamini, L. A. Kavoussi, and J. H. Anderson, "A telerobotic assistant for laparoscopic surgery", *IEEE EMBS Mag.*, vol. 14, no. 3, pp. 279–291, 1995.

[11] A. C. Waspe, H. J. Cakiroglu, J. C. Lacefield, and A. Fenster, "Design, calibration, and validation of a robotic needle positioning system for small animal imaging applications", *IEEE Trans. Robot.*, submitted for publication.

[12] G. Wan, Z. Wei, L. Gardi, D. B. Downey, and A. Fenster, "Brachytherapy needle deflection evaluation and correction", *Med. Phys.*, vol. 32, no. 4, pp. 902–909, 2005.

[13] F. S. Foster, M. Y. Zhang, Y. Q. Zhou, G. Liu, J. Mehi, E. Cherin, K. A. Harasiewicz, B. G. Starkoski, L. Zan, D. A. Knapik, and S. L. Adamson, "A new ultrasound instrument for in vivo microimaging of mice", *Ultrasound Med. Biol.*, vol. 28, no. 9, pp. 1165–1172, 2002.

[14] A. Fenster, D. B. Downey, and H. N. Cardinal, "Three-dimensional ultrasound imaging", *Phys. Med. Biol.*, vol. 46, no. 5, pp. R67–R99, 2001.

[15] D. W. Holdsworth, and M. M. Thornton, "Micro-CT in small animal and specimen imaging", *Trends Biotechnol.*, vol. 20, no. 8, pp. S34–S39, 2002.